CRYSTAL GROWTH & DESIGN

pubs.acs.org/crystal

Article



# Gravity as a Knob for Tuning Particle Size Distributions of Small Molecules

Kanjakha Pal and Adrian Radocea*

Cite This: https://doi.org/10.1021/acs.cgd.3c01274

Read Online

ACCESS | Metrics & More | Article Recommendations | Supporting Information

**ABSTRACT:** Pharmaceutical research and development and manufacturing can widely benefit from a microgravity environment. Although the use of microgravity to improve control over the size of protein crystals has been demonstrated, there have been few studies on the effect of gravity on small molecules. A hypergravity crystallization platform was developed as a rapid screening tool for the crystallization of small-molecule pharmaceuticals. This platform was used to show the effect of gravity on the nucleation and growth kinetics of L-histidine. Further experiments were conducted in the EasyMax reaction calorimeter with process analytical technology (PAT) tools to understand the kinetics of nucleation and growth and quantify the desupersaturation rate in the seeded cooling crystallization experiment.

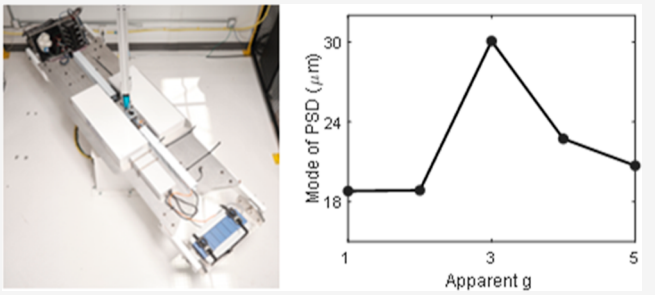




## 1. INTRODUCTION

Microgravity crystallization studies of therapeutic antibodies[1] demonstrate that reduced gravity environments enable improved control over particle size, unlocking new formulations for drug delivery. While past challenges encountered during crystallization of antibodies have barred incorporation of crystallized products[2] into commercial pipelines alongside noncrystalline suspensions and ready-made solutions,[3] increased access to space is now changing the developmental landscape for drug development. Today, pharmaceutical and drug manufacturers are increasingly investigating the benefits of microgravity for drug development of crystallized therapeutics.[4−6] Microgravity crystallization provides many potential benefits in industries like pharmaceuticals,[7] personal care, semiconductors, and food processing.[8]

In contrast to biologics, small-molecule therapeutics already rely on crystallization[9] as one of the most important unit operations at the intersection of both drug substance and drug product manufacturing. One of the most widely used modes of crystallization in industry is cooling crystallization.[10] During cooling crystallization, the temperature is used to generate the supersaturation necessary to crystallize the molecules from the solution. The solubility of most pharmaceutical molecules decreases with temperature.[11] Thus, cooling the solution reduces the solubility, thereby increasing the supersaturation, which is the driving force for crystal nucleation and growth. There are two major modes of cooling crystallization—unseeded[12] and seeded[13] cooling crystallization. In contrast to unseeded crystallization, seeded cooling crystallization[14] is more robust and well-controlled and is thereby widely used in the pharmaceutical industry. Various micrometric properties such as particle shape[15] and size[16] can be controlled by implementing the desired cooling profiles during batch cooling crystallization. Control over crystal and particle properties is critical for both the manufacturability and bioavailability of drug compounds.[16,17]

Increased access to space has presented a renewed opportunity to conduct pharmaceutical development in orbit,[18] largely due to the commercialization of reusable rockets.[19] With in-space drug development increasingly feasible, rapidly advancing knowledge and understanding of how gravity impacts drug development processes, such as crystallization, can create great benefit. While recent advances achieved in space-based drug development build on foundational knowledge of protein crystallization developed onboard space stations for decades,[20,21] microgravity crystallization of small molecules has been less explored. Variable gravity platforms can serve an important role in generating data sets that measure the impact of gravity to better inform both space and conventional crystallization development programs.

While gravitational forces do not directly impact the thermodynamic properties of systems,[22] kinetic and hydrodynamic processes are significantly altered.[23] Reducing gravity suppresses convection and sedimentation, resulting in diffusion-driven transport and a reduction of crystallization rates.[24] In contrast, hypergravity environments achieved

Received: October 26, 2023
Revised: February 21, 2024
Accepted: February 26, 2024

through increased centrifugal forces often increase crystallization rates through gravity-induced concentration gradients that alter local supersaturation to overcome kinetic barriers.[25] Centrifugation has been shown to increase the nucleation rate of aptoferritin,[26] alter the morphology of tomato bushy stunt virus (TBSV), lysozyme, and thaumatin crystals, while also altering their nucleation and growth rates as exhibited by a 9-fold increase in the growth rate of TBSV single crystals.[25] Hypergravity has also been shown to change the morphology of particles in other fields, e.g., semiconductor nanocrystals.[27] To date, the majority of hypergravity crystallization studies have observed differences at more than 100 g, as exhibited by a previous study of lysozyme that showed no observed changes in crystallization rates at low g-levels.[28] In contrast to previous hypergravity studies that examine the crystallization of proteins and inorganic materials at high g-levels, this work investigates the crystallization of a small molecule in the 1 to 5 g range.

A large diameter centrifuge was constructed at Varda for hypergravity studies, which aims to measure the effect of the g level on product particle size distributions (PSDs). Seeded cooling crystallization experiments were designed and conducted on a Crystal16 (Technobis Crystallization Systems) reactor at different g-levels. This was followed by further targeted experiments in an EasyMax reaction calorimeter fitted with process analytical technology (PAT)[29] tools to understand the fundamental mechanisms underlying the sensitivity of the cooling crystallization to increasing g-levels.

There are a few fundamental mechanisms underlying each crystallization process, e.g., primary nucleation, secondary nucleation, and growth. In addition to crystallization, breakage and agglomeration also occur in industrial crystallizers. Primary nucleation is the spontaneous appearance of nuclei in a supersaturated solution. The critical temperature needed to cause primary nucleation is called the nucleation threshold, and the region of the phase diagram between the solubility curve and the nucleation threshold is called the metastable zone. Most industrial seeded crystallization processes aim to stay within the metastable zone to avoid primary nucleation (a stochastic process). Within the metastable zone, secondary can occur via surface breeding,[30] shear,[31] and attrition.[32] The rates of secondary nucleation and growth are both dependent on instantaneous supersaturation. Since the rate of cooling determines instantaneous supersaturation, it also determines the relative rates of secondary nucleation. Simultaneously, breakage and attrition of crystals in the solution can occur due to particle-impeller, particle-wall, or particle−particle interactions. Breakage and attrition can both lead to a shift in the PSD; however, breakage/attrition conserves the total mass of solids during the crystallization, while secondary nucleation and growth lead to increased solids mass.

## 2. METHODS

**2.1. Chemicals.** L-Histidine (>99% TLC) was obtained from Sigma-Aldrich (CAS number 71-00-1). Deionized water was obtained by using an in-house purification system. Reagent alcohol (anhydrous ethanol 90%, methanol 5%, 2-propanol 5% v/v) was obtained from Fisher Scientific as a solvent for PSD analysis for laser diffraction.

**2.2. Seed Preparation.** L-Histidine as received from the supplier was sieved using a stack of sieves (500, 250, 125, 63 $\mu$m, pan). After sieving, the sieve fraction obtained from the 125 $\mu$m sieve was used as the source for seed crystals for the hypergravity experiments. The PSD of the seed crystals was analyzed using the laser diffraction method described in Section 2.6.

**2.3. Solubility.** The solubility of L-histidine in water was measured using the polythermal technique outlined by Barrett and Glennon.[33] Focused beam reflectance measurement (FBRM) is an online tool to measure the chord length distribution (CLD) of particles in real time during the crystallization process. A slurry of a known concentration was prepared in the EasyMax reactor[34] with the FBRM probe inserted and equilibrated at a constant temperature. The slurry was then heated at a constant rate until the crystals disappeared which was detected by a reduction in counts/s with the FBRM. The process was repeated at different heating rates (0.1, 0.25, 0.4, and 0.55 °C/min), and the temperature of disappearance at each of the heating rates was recorded. The saturation temperature was calculated by extrapolating the temperature of the disappearance data to a 0 °C/min heating rate. The entire process was repeated at different solid concentrations to obtain the solubility temperature at different solid concentrations. The solubility curve was then determined from regression analysis in Excel.

**2.4. MSZW Using the EasyMax Reactor.** Experiments to determine the metastable zone width (MSZW)[33] were conducted in an EasyMax reactor (Mettler Toledo Inc.) equipped with a pitched blade turbine impeller. The impeller was stirred at 200 rpm for all of the experiments. The reactor was equipped with a Blaze900 Basic probe[35] which was used to measure the evolution of the CLD, perform real-time microscopy during cooling crystallization, and determine the MSZW. The reactor was also equipped with a Raman probe, which was used for the measurement of concentration in real time during the crystallization.

For the MSZW measurements, a saturated solution was cooled slowly until the high dynamic range (HDR) turbidity provided by the Blaze software showed an inflection, indicating the formation of fine particles in the solution. The solution was typically heated to 5 °C above its saturation temperature and then cooled down to 10 °C at 0.05 °C/min. The process was repeated at different API concentrations corresponding to different saturation temperatures.

**2.5. Optical Imaging.** Optical images were taken using an optical stereo microscope (model M205C from Leica Microsystems). The field of view of the microscope is in the range of 1.44−29.5 mm, and the resolution is in the range of 525 and 1050 lp/mm. The zoom range of the microscope is 20.5:1, and a K3C CMOS camera from Leica is used to capture optical micrographs.

**2.6. Particle Size Distribution Measurement by Laser Diffraction.** The PSD of the particles was measured by using laser diffraction (LS13320, Beckman Coulter). The instrument uses a 5 mW laser diode with a wavelength of 750 nm as the main illumination source. Reagent alcohol (anhydrous ethanol 90%, methanol 5%, 2-propanol 5% v/v), in which L-histidine is insoluble, is used as the dispersant for the laser diffraction measurements. The raw data obtained from the laser diffraction instrument is the volume % vs particle size. However, this distribution is postprocessed to calculate the PSD (vol %/$\mu$m) following eq 1.

$$f_v\ (\text{vol}\ \%/\mu\text{m}) = \frac{N_v\ (\text{vol}\ \%)}{\Delta x} \tag{1}$$

**2.7. Seeded Cooling Crystallization Experiments on EasyMax.** A saturated solution of L-histidine in water at 40 °C was prepared by dissolving the requisite amount of L-histidine in water. The solution was heated to 60 °C to ensure complete dissolution, which was also confirmed by the counts/s measured by the Blaze probe. The solution was then cooled to 32.8 °C as fast as possible to bring the system into the metastable zone, corresponding to a supersaturation of 1.2. The supersaturation ratio (SS) is calculated according to eq 2, where $C$ ($g_{solute}/g_{solvent}$) is the solute concentration and $C_{sat}$ ($g_{solute}/g_{solvent}$) is the saturation concentration.

$$\text{SS} = \frac{C\left(\frac{g_{solute}}{g_{solvent}}\right)}{C_{sat}\left(\frac{g_{solute}}{g_{solvent}}\right)} \tag{2}$$


https://doi.org/10.1021/acs.cgd.3c01274
Cryst. Growth Des. XXXX, XXX, XXX−XXX

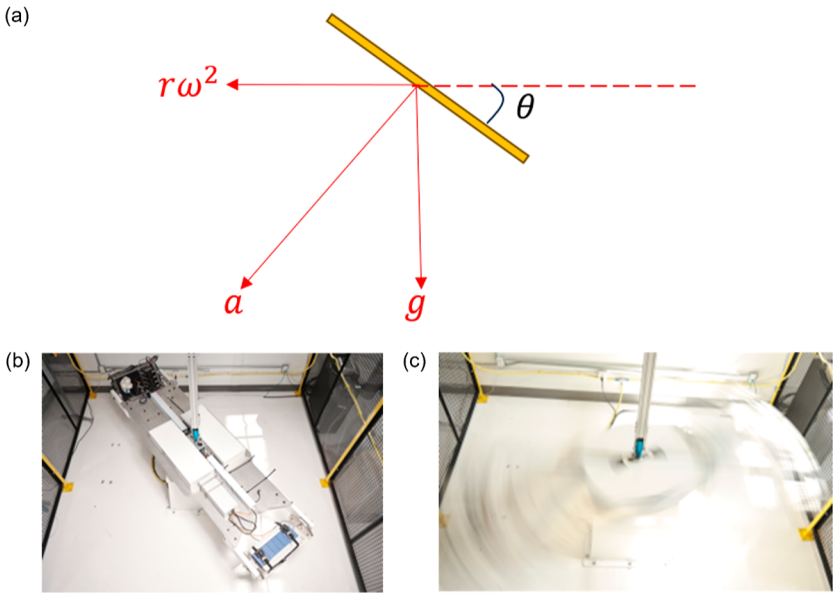


**Figure 1.** (a) Illustration of the net force experienced during crystallization, which is the vector sum of the gravitational force and the centrifugal force. (b) Photographs of the centrifuge, which features a tiltable basket at rest and (c) in motion.

Seed crystals (10% by weight of solute in solution) were then added to the reactor, and the solution was kept at 32.8 °C for 5 min for slurry equilibration. The solution was then cooled to 18.0 °C at 0.1 °C/min. After the experiment, the solution was filtered using a 0.2 $\mu$m Nylon filter (Cole Palmer), followed by washing with a wash solvent (95% ethanol and 5% water). This was followed by drying the filtrate at 40 °C for 12 h.

**2.8. Centrifuge Experiments.** Experiments were conducted on a centrifuge built in-house with an arm length of 1.574 m. All cooling crystallization experiments were performed on a Crystal16 reactor (Technobis Crystallization Systems). The Crystal16 was mounted at the end of the arm on the centrifuge. The centrifuge rotates along its axis at defined rotations per minute (rpm). During the centrifuge rotation, the Crystal16 reactor is housed in a basket with an adjustable tilt to align the vial axis with the apparent gravity vector, which is a function of the rpm, the radius of the arm, and the earth's gravity vector. A picture of the setup is shown in Figure 1.

The net acceleration in the centrifuge is given by eq 3, where $g$ is the gravitational acceleration, $\omega$ is the rotation speed of the centrifuge, and $r$ is the radius of the centrifuge arm. The angle for the effective gravitational force is given in eq 4.

$$a = \sqrt{g^2 + (\omega r)^2} \tag{3}$$

$$\theta = \tan^{-1}\left(\frac{g}{\omega^2 r}\right) \tag{4}$$

The rotational speed is changed to obtain the desired effective gravitational force. The rotation speed can be calculated from eq 3 and the angle of the effective gravitational force is given by eq 6. An overview of the net acceleration vector and the effective angle is shown in Figure 1a.

$$\omega = \frac{\sqrt[4]{a^2 - g^2}}{\sqrt{r}} \tag{5}$$

$$\theta = \tan^{-1}\left(\frac{g}{\sqrt{a^2 - g^2}}\right) \tag{6}$$

It is to be noted that there is a risk of vibrations on the centrifuge influencing the outcome of the crystallization experiments. However, since the solution is stirred during the process, the risks of vibrations influencing the process are very low and are not considered while analyzing the resulting PSD of the process.

**2.9. Seeded Cooling Crystallization on Centrifuge.** Three of the Crystal16 slots within a reactor were used for each experiment for obtaining repeats for each experiment. Cylindrical bottom magnetic stirrers with diameters of 0.03 in. and length of 0.27 in. were used for the experiments unless otherwise mentioned. The Crystal16 reactors were stirred at 800 rpm to match the tip speed with the experiments conducted in the EasyMax reactor. The volume of the API solution dispensed into each vial was 2 mL. A saturated API solution at 40 °C was first prepared by dissolving the requisite quantity of L-histidine in water in a vial in the laboratory, followed by pipetting 2 mL of the saturated API solution into the HPLC vial and then inserting the magnetic stirrer into the bottom of the vial. The capped HPLC vials were then transferred to the slots of the Crystal16 reactor for crystallization experiments.

The solution was then heated in the Crystal16 to 60.0 °C to ensure complete dissolution of the solids. The solution was stirred at 800 rpm by using a magnetic stir bar kept at the bottom of the vial. The transmittance in the Crystal16 vial was recorded to ensure all of the particles were dissolved. Simultaneously, the centrifuge was rotated at the desired rotations per minute (rpm), corresponding to the effective g-level desired in the experiment. The relationship between rpm and the effective g-level is provided in Table 1. At the end of the experiment, the vials were removed from the Crystal16 reactor for particle size analysis. An overview of the entire process is given in Figure 2.

**Table 1. Calculated g-Levels and Corresponding rpm**

| effective g-level | rpm |
|---|---|
| 2 | 31 |
| 3 | 40 |
| 4 | 47 |
| 5 | 53 |

**2.10. Dissolution Experiments on Centrifuge.** An L-histidine solution saturated at 24 °C was prepared and pipetted into 2 mL vials for the Crystal16 experiments. The vials were then inserted into the sample holders in the Crystal16 reactor and were equilibrated at 24 °C. The solution was stirred at 800 rpm throughout the experiment. Seed crystals (10% w/w) were then poured into the vials, followed by slow heating from 24 to 28 °C at 0.1 °C/min over 40 min.


https://doi.org/10.1021/acs.cgd.3c01274
Cryst. Growth Des. XXXX, XXX, XXX−XXX

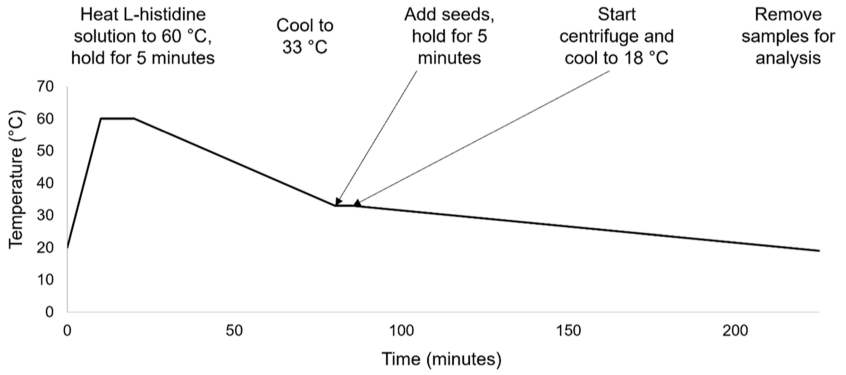


**Figure 2.** Experimental protocol used for seeded crystallization experiment with Crystal16 on a centrifuge.

Simultaneously, the centrifuge was spun at the desired rpm corresponding to the g-level in Table 1. The centrifuge and the Crystal16 apparatus were simultaneously stopped at 20 min to withdraw the first sample. This step was followed by restarting the centrifuge and the Crystal16 reactor and running the experiment for another 20 min. The PSDs of the samples withdrawn at 20 and 40 min during the dissolution experiment were analyzed using laser diffraction.

## 3. RESULTS AND DISCUSSION

In the following three sections, we will map the process window for the seeded cooling crystallization experiment in the EasyMax reactor with a top-down pitch blade turbine (PBT) impeller. We first map the MSZW and solubility, develop a chemometric model to monitor concentration, and then run seeded desupersaturation experiments to distinguish between primary nucleation, secondary nucleation, and breakage.

**3.1. Solubility and MSZW.** Slurries of L-histidine were prepared at 8 °C in water in the EasyMax reactor and stirred at 300 rpm. Five different slurries of different solid concentrations (0.035, 0.0415, 0.0479, 0.0545, and 0.0601 g/g) were used for the experiments. The disappearance temperature of the slurry was calculated using the polythermal method outlined in Section 2.3. Figure S6a−e shows the disappearance temperatures of the slurries at different solid concentrations for polymorph A of L-histidine. A second-order polynomial is used to calculate the solubility curve from the experimental measurements of the solids concentration vs disappearance temperature and is shown in Figure 3a. The solubility calculated from these experiments agrees well with the literature reports.[36]

The MSZW is one of the critical process parameters that define the crystallization process. The metastable zone was identified using a probe-based technique (Blaze probe). 100 mL aliquot of a saturated L-histidine solution was stirred in the EasyMax reactor (Mettler Toledo) at 200 rpm. Since the agitator used in the EasyMax has a larger diameter, the rpm needs to be lower to maintain a similar tip speed compared to the bottom stirrer in the Crystal16. The solution was heated to 10 °C above its saturation temperature to ensure complete dissolution. This was followed by slow cooling at 0.1 °C/min to 18 °C. The particle counts/s in the solution were monitored using the Blaze probe throughout the process. The point of nucleation is registered as a sudden increase in the counts/s, which corresponds to the primary nucleation threshold. It should be noted that while the laser diffraction data in Section 3.4 plots a normalized volumetric distribution, this section discusses counts/s, and readers comparing the visual

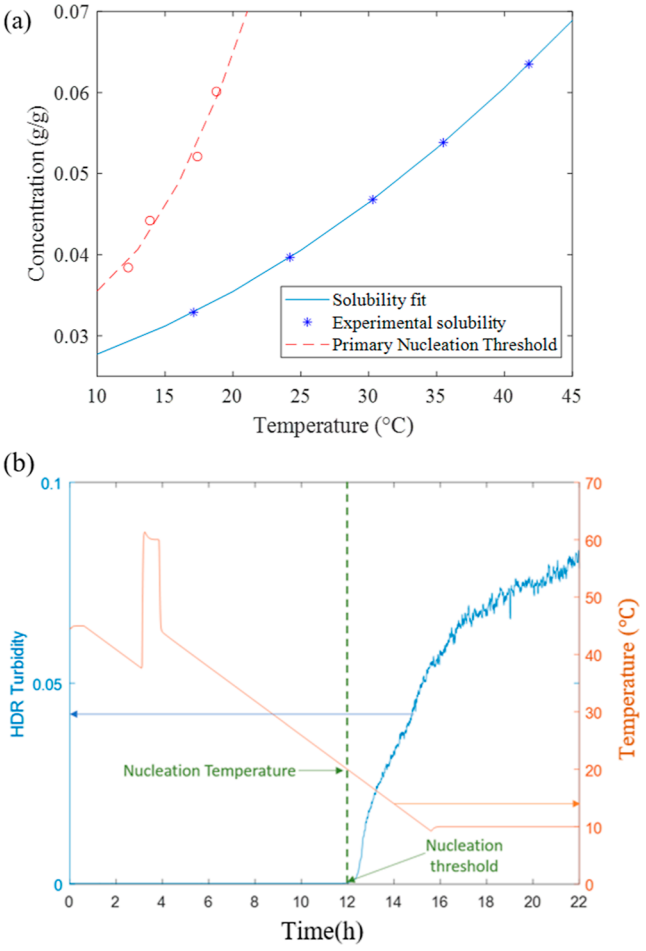


**Figure 3.** (a) Solubility and MSZW of L-histidine cooling crystallization in water. (b) Temperature, HDR turbidity, and nucleation temperature in the crystallizer for MSZW determination experiments.

appearance of the plots should not expect a 1:1 relative peak height due to the nature of the axes being plotted.[37] The process is repeated at different L-histidine concentrations to find the metastable zone over the entire range of temperatures. The increase in the HDR turbidity with cooling at the nucleation threshold (18.78 °C) for L-histidine at a concentration of 0.06 mg/mL is shown in Figure 3a. The nucleation temperature is the temperature at which the HDR curve is recorded with an inflection. The metastable zone as a function of the temperature is plotted in Figure 3b, along with


https://doi.org/10.1021/acs.cgd.3c01274
Cryst. Growth Des. XXXX, XXX, XXX−XXX

the solubility curve in the phase diagram. Although there are previous literature reports which have characterized the induction time/nucleation rates for the cooling crystallization of L-histidine,[38] to the best of the authors' knowledge, there have not been previous reports in the literature that have characterized the MSZW of L-histidine for cooling crystallization in water. There have been some reports on the characterization of MSZWs during antisolvent crystallization experiments.[39] However, since the MSZW depends on the solvent system, the MSZW reported in the literature does not transfer directly to cooling crystallization experiments.

**3.2. Chemometric Modeling.** To fully characterize the crystallization process, one needs to track the evolution of the particle size and the solute concentration during the crystallization process. The Blaze probe can provide information on how the CLD changes in the solution with time, which can provide information about fundamental mechanisms. However, it is also necessary to follow the evolution of the system in the phase diagram and quantify whether the system crosses the MSZW during the operation. The Raman spectra are a function of the solute concentration and temperature; therefore, a chemometric model was built to calculate the solution concentration from the in situ measurements of Raman spectra at variable temperatures. The experimental data used for MSZW determination can be used directly for building the chemometric model and is shown in Figure 3b. The Raman spectra are shown in Figure S4. A zoomed-in version of the spectra is shown in Figure 4a with the major spectral peaks. Both univariate and multivariate methods can be considered for building a chemometric model.[40−42] The time evolution of all the peaks was thoroughly analyzed, and a subset of peaks were chosen that are most sensitive to change around the time when nucleation occurs. Figure 4b indicates that the peaks around 1286, 1440, 1160, and 990 $cm^{-1}$ have a reduction in peak height around the time nucleation occurs (12 h), which are indicative of peaks that correspond to L-histidine molecules in solution. However, peaks around 1323 and 1088 $cm^{-1}$ show an increase in peak height around 12 h, which is indicative of peaks corresponding to the solid phase. For monitoring the concentration of L-histidine in solution, the first subset of peaks is chosen for further analysis.

The Raman spectra were postprocessed using ICRaman software from Mettler Toledo before being exported to Matlab for building the chemometric model. SNV scatter correction and Pearson's-like baseline correction, which adjusts spectra to a straight baseline, were applied to the spectra, followed by smoothing over a 10 $cm^{-1}$ window. A total of 1356 spectra were used for the analysis. No spectral outliers were detected during the model calibration. The chemometric model calibration pipeline was run for all four peaks, and the goodness of fit for the four peaks is shown in Table 2. The goodness of fit is lower for peaks with a Raman shift of 1160 and 990 $cm^{-1}$ and is hence not used for further analysis. The strategy employed in this work is to proceed with the model calibration with only one peak in the chemometric model. The Raman peak with the highest $R^2$ in Table 2 (1286 $cm^{-1}$) was chosen for further analysis. The chemometric model[41,42] is shown in eq 7, where $h$ is the peak height and $T$ is the temperature. This model describes the peak height in the Raman spectra as a function of the L-histidine concentration and solution temperature.

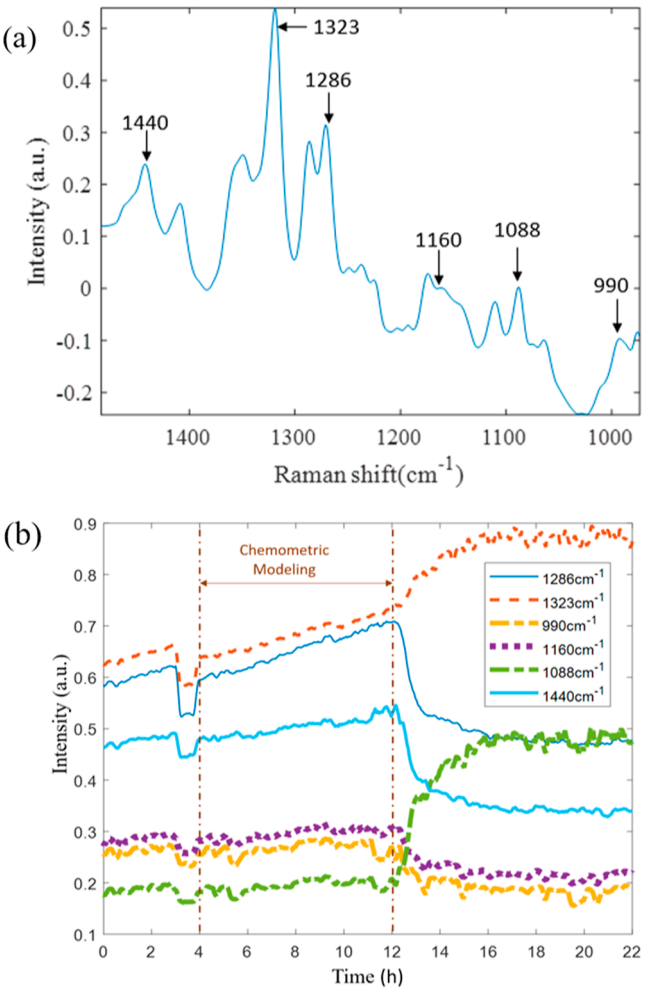


**Figure 4.** (a) Raman spectra of L-histidine in water with major peaks. (b) Tracking peaks in the Raman spectra with time.

**Table 2. Goodness of Fit for Chemometric Model Calibration for Different Peaks in the Raman Spectra**

| Raman shift ($cm^{-1}$) | $R^2$ (calibration) |
|---|---|
| 1286 | 0.9938 |
| 1440 | 0.9915 |
| 1160 | 0.9710 |
| 990 | 0.9142 |

$$C = a_1 + a_2h + a_3T + a_4hT + a_5h^2 \quad (7)$$

The model calibration is carried out using a custom-written script in Matlab R2023a. Linear regression is carried out in Matlab using the function mldivide[44] which solves a system of linear equations from which the coefficients in eq 7 are determined, followed by determination of goodness of fit for the model. The coefficients for the chemometric model calibration (for a Raman shift of 1286 $cm^{-1}$) in eq 7 are shown in Table 3.

The time-course evolution of the peak height, temperature, and L-histidine concentration are shown in Figure 5. L-Histidine concentrations are constant for each of the five experiments in Figure 5b since the region prenucleation has been analyzed. The peak height (Figure 5a) increases with the decrease in temperature (Figure 5c) for each of the five experiments. This indicates that the peak height is a function of


https://doi.org/10.1021/acs.cgd.3c01274
Cryst. Growth Des. XXXX, XXX, XXX−XXX

**Table 3. Coefficients from the Chemometric Model in Eq 7 (Raman Shift of 1286 $cm^{-1}$)**

| coefficient | value |
|---|---|
| $a_1$ | 0.0267 |
| $a_2$ | 0 |
| $a_3$ | −0.0013 |
| $a_4$ | 0.0032 |
| $a_5$ | 0.0320 |

the L-histidine concentration and the temperature, which adds validity to the functional form of the chemometric model in eq 7. Figure S8 shows the distribution of the predicted concentration for each of the data points used in the chemometric model. It can be seen that the distributions are very narrow around their means, and there is no overlap in the distributions. The coefficients of variation (standard deviation/mean) of the predicted concentrations for the five different L-histidine concentrations are 1.2, 2.4, 1.3, 1.5, and 1.6% respectively. The average coefficient of variation (1.6%) is less than 5% for all experiments, which illustrates that the chemometric model is accurately fitting the experimental data. However, if the COV of the predicted L-histidine concentration was not less than 5%, PLSR models could have been used alternatively.[41,42]

To validate the goodness of fit, a validation experiment was run with a L-histidine concentration of 54.5 mg/mL L-histidine following a similar experimental protocol. The saturated L-histidine solution was cooled until nucleation, and the experimental data before nucleation were chosen for model validation. The coefficients evaluated in the model (7) were used to calculate the predicted L-histidine concentration. Figure 6a shows the time-course evolution of the temperature and peak height from the L-histidine spectra before nucleation occurs. The peak height decreases with an increase in temperature, similar to the calibration experiments (Figure 5a–c). Figure 6b compares the evolution of the predicted L-histidine concentration to the actual L-histidine concentration during the validation experiment. The mean of the predicted concentration value for the validation experiment was 54.7 mg/mL, and the adjusted $R^2$ was 0.897. The coefficient of variation for the model predictions in Figure 6b is 2.54%.

**3.3. Seeded Desupersaturation Experiments (EasyMax).** Seeded desupersaturation experiments were run in the Mettler Toledo EasyMax 102 reactor. 100 mL of L-histidine solution saturated at 40.0 °C was heated to 60.0 °C to ensure complete dissolution. The solution was stirred at 200 rpm throughout the process. The solution was then cooled to 32.8 °C to bring the system into the metastable zone for seeding. This corresponded to a supersaturation ratio of 1.2 during seed addition. Seed crystals (10% w/w of total mass of solute) were added to the solution and stirred for 5 min to form a spatially homogeneous seed bed. This is followed by implementing the temperature profile, which causes desupersaturation of the L-

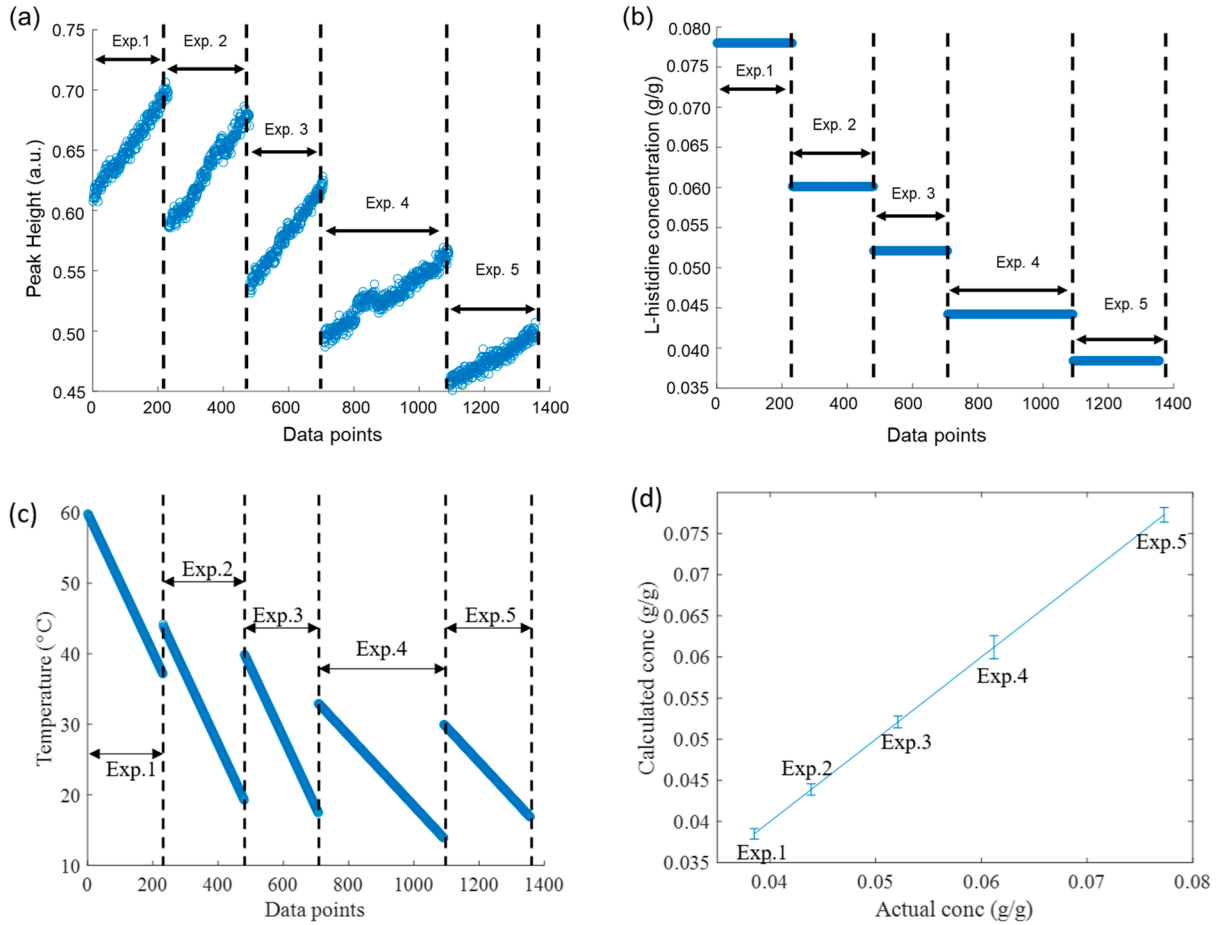


**Figure 5.** (a) Peak height from L-histidine spectra, (b) experimental L-histidine concentration, (c) temperature, and (d) predicted vs actual concentrations from the chemometric model.


https://doi.org/10.1021/acs.cgd.3c01274
Cryst. Growth Des. XXXX, XXX, XXX−XXX

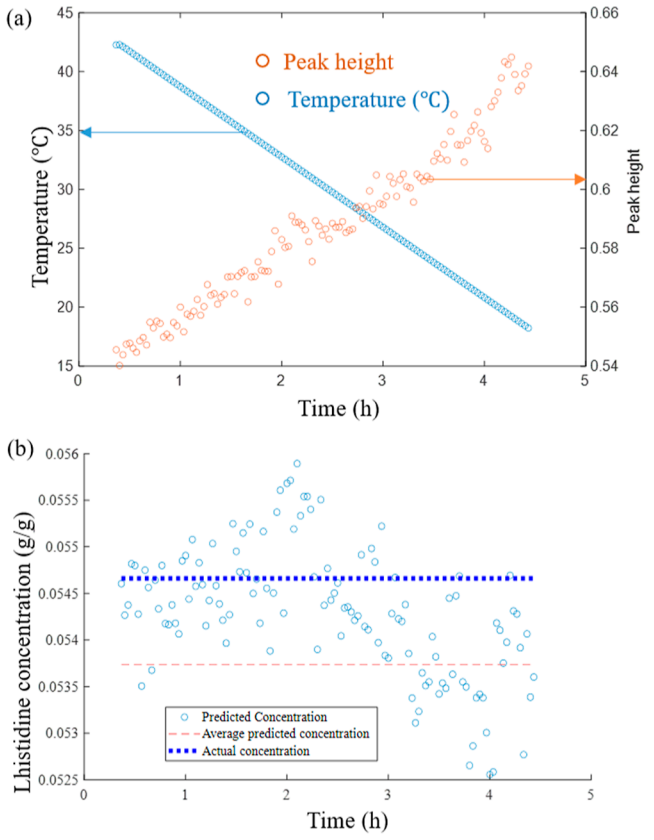


**Figure 6.** (a) Temperature and peak height ($cm^{-1}$) vs time for validation experiment. (b) Predicted L-histidine concentration vs actual L-histidine concentration for validation experiment.

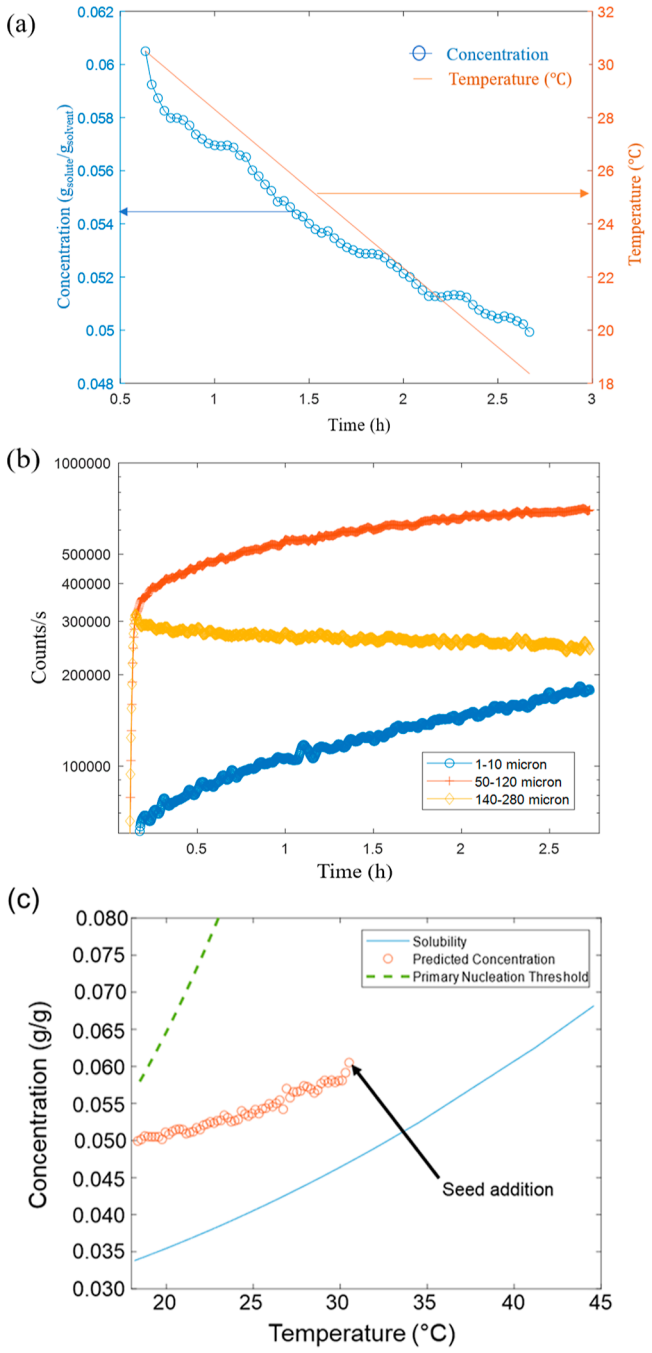


**Figure 7.** (a) L-Histidine concentration and temperature evolution. (b) Evolution of total counts/s with *y*-axis on a logarithmic scale. (c) Evolution of concentration in the phase diagram for seeded cooling crystallization experiments with L-histidine.

histidine solution. The Raman spectra and temperature profiles collected during the experiment were postprocessed using Matlab. The chemometric model built in Section 3.2 is then applied to the Raman spectra to estimate the L-histidine concentration. The evolution of the L-histidine concentration along with the solution temperature is shown in Figure 7a. The L-histidine concentration reduces quickly until 1.1 h, followed by a slower decrease in concentration until 2.5 h. The crystal growth rate coefficient of many APIs follows Arrhenius dependence on temperature, leading to faster kinetics with increasing temperature.[43] As a result, cooling crystallization can exhibit high initial growth rates and desupersaturation rates which decrease over time as the reactor temperature is lowered. The evolution of the counts/s recorded in the Blaze probe is shown in Figure 7b. The *y*-axis of Figure 7b is plotted on a logarithmic scale to exemplify the differences in the evolution of counts/s for the three different size ranges (1−10, 50−120, and 140−280 $\mu$m). The fine particle counts (1−10 $\mu$m) increase rapidly during crystallization, while the coarse particle counts (140−280 $\mu$m) remain relatively stable. The stability in particle counts for large particles corresponding to the seed crystals (140−280 $\mu$m) suggests that breakage is unlikely to be playing a role. The evolution of the system in the concentration phase diagram is shown in Figure 7c. The system stays within the metastable zone, which rules out primary nucleation and points to secondary nucleation and growth as the dominant mechanisms during the desupersaturation experiment. The pH of the solution was the same before and after the experiment (Table S1 in Supporting Information), which shows that L-histidine did not undergo deprotonation.

The CLD data from the Blaze probe was postprocessed with a Matlab script. The recorded length-weighted and cube-weighted CLDs were extracted at defined time points and plotted with the Matlab script and are shown in Figure 8g,h. Images from the Blaze probe were also analyzed to elucidate the dominant mechanism during desupersaturation. At 0.57 h (Figure 8b), secondary nuclei on the surface of the crystals can be seen in the image obtained from the Blaze probe. The images from 0.87 to 2.5 h (Figure 8c−f) also indicate that


https://doi.org/10.1021/acs.cgd.3c01274
Cryst. Growth Des. XXXX, XXX, XXX−XXX

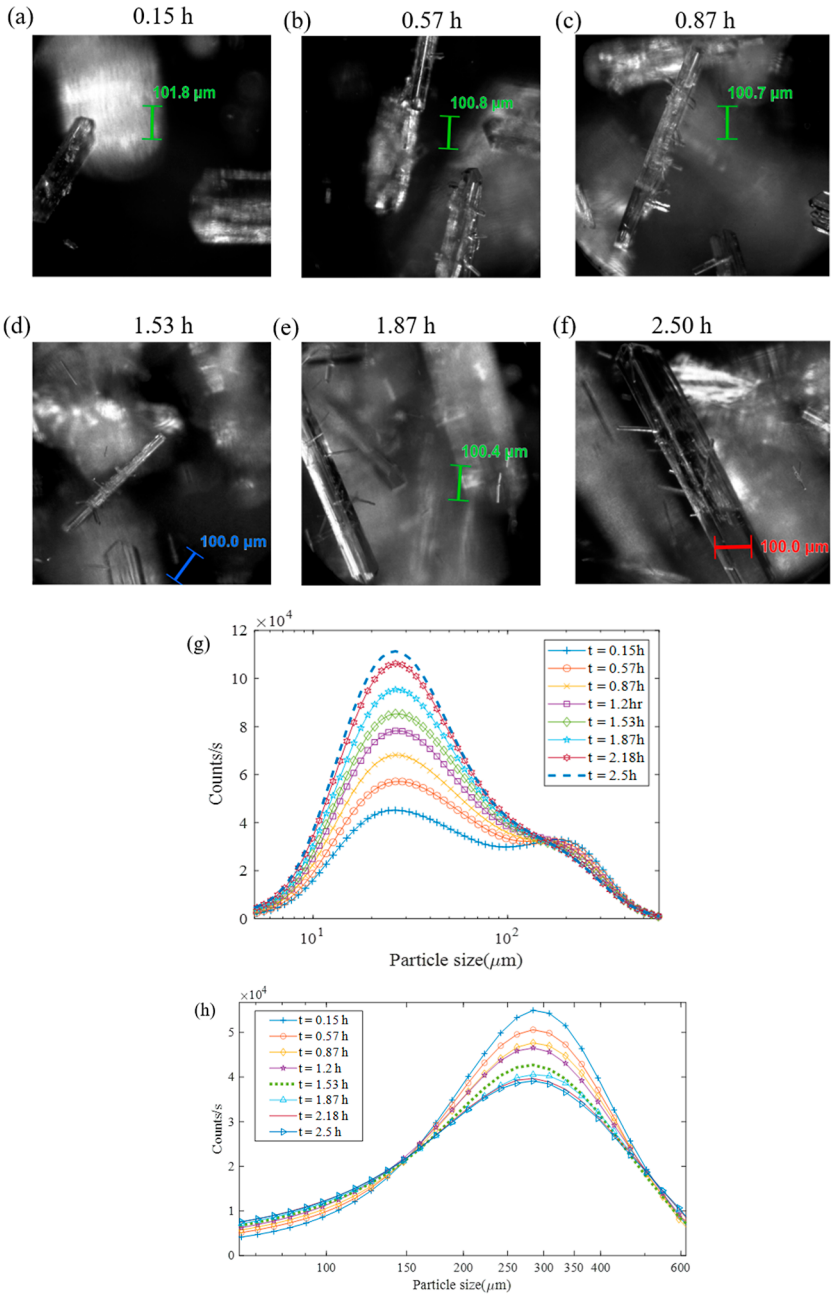


**Figure 8.** (a–f) In situ images obtained from the Blaze probe. Evolution of (g) length-weighted CLD, and (h) cube-weighted CLD throughout the seeded cooling crystallization process.

secondary nuclei are present and do not indicate growth of the needles along the lateral direction. The evolution of the length-weighted chord length distribution (LWCLD) in Figure 8g also shows that the rate of increase of the counts/s is much slower during 2.18–2.5 h compared to the earlier parts of the experiment. This indicates slower desupersaturation during the last part of the experiment, which is corroborated by the slower concentration decrease in Figure 8 from 2.2 to 2.5 h. As exhibited in Figure 8g, seed crystals are still present in the final LWCLD, but they are overshadowed by the high proportion of smaller crystals in the product samples.

Figure 8h also shows the evolution of the cube-weighted chord length distribution (CWCLD) throughout the experiment. The CWCLD in the Blaze probe biases the CLD toward coarser particles. It is to be noted that the CWCLD distribution is equivalent to the square-weighted chord length distribution (SWCLD) in the FBRM.[45] Thus, the evolution of the CWCLD in the process is a representation of the evolution of coarser particles in the process. If breakage had been the only dominating mechanism, the larger particles would have broken down into smaller particles.[46,47] Breakage is characterized by a shift of the mode of the CWCLD to the left with time, which is not observed in Figure 8g. In contrast, during secondary nucleation, the generation of many fine particles increases the total counts/s in the LWCLD with time. The evolution of the LWCLD in the process (Figure 8g) is most representative of secondary nucleation,[48] which confirms that secondary nucleation is the dominant mechanism in the EasyMax experiments. In addition, the final mass of the filtered crystals (1.45 g) is much higher than the seed crystal mass (0.6


https://doi.org/10.1021/acs.cgd.3c01274
Cryst. Growth Des. XXXX, XXX, XXX–XXX

g), which cannot be attributed to breakage alone and can only be caused by secondary nucleation and/or growth. To examine the evolution of the seed particles during the experiment, the average circularity of the seed and product crystals was calculated from dynamic image analysis and indicated little change in the shape of the seed particles (Figure S5). Figure 8 is typical of a crystallization process dominated by secondary nucleation and growth, where both processes occur with a similar driving force, e.g., the supersaturation consumption due to nucleation and growth is comparable.

**3.4. Effect of Apparent g-Level.** In this section, we run the L-histidine experiment developed on the EasyMax at the 2 mL scale on the Crystal16. Laser diffraction measurements were used to measure the PSD of the obtained crystallization products at a range of g-levels, and we interpreted the observed peaks. We ran additional experiments to rule out breakage, primary nucleation, and other effects.

Figure 9 shows the evolution of the volume-based PSD[49] with changes in g-levels at a cooling rate of 0.1 °C/min. All the

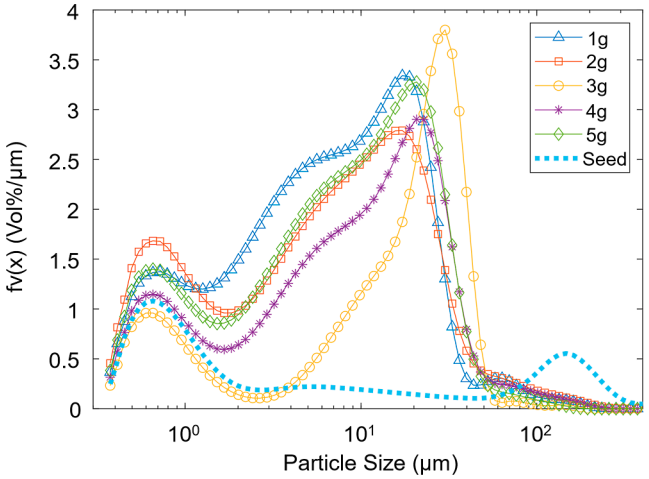


**Figure 9.** Volume-based PSD for different g-levels at a cooling rate of 0.1 °C/min.

samples, except the seed crystals, are those obtained at the end of the desupersaturation experiment. The apparent g-level has a marked effect on the PSD of the samples. There are three distinct peaks to consider across the seed and product PSDs—one around 0.7 μm, a second peak around 20−30 μm, and a third peak at 180 μm. It should be noted that Figure 9 is a volume-based distribution of the filtered samples and cannot be directly compared to Figure 8g, which is a number-based distribution of samples measured in situ.

The peak at 0.7 μm is present in the seed PSD, as well as in the product samples. The appearance of the 0.7 μm peak could be attributed to the presence of fine particles which were either (a) stuck on the screen during the sieving process along with the larger seed crystals, possibly due to screen blinding, or (b) were attached to the seed particles during sieving and got detached when seed crystals were dispersed into the solution. Alternatively, the 0.7 μm peak may correspond to the shortest dimension of crystals present in the sample population. However, when the un-normalized volume fraction is plotted vs the particle size (Figure S1), the total volume fraction of the fines is low (less than or equal to 1.8%) for each seed and product sample. Since the total volume fraction of the peak around 0.7 μm does not change significantly between the seeds and the product (Figure S1), it is unlikely to be a result of crystal growth or attrition during the experiment.

Though the peak around 180 μm is not evident in the normalized volume-based product PSD, particles in the size range of 180 μm are expected to be present as confirmed with optical imaging and previously in Section 3.3. The volume fraction of the seed crystals is overshadowed by the volume fraction of the product crystals in the normalized distributions plotted in Figure 9. For further clarification, the volume fraction distribution measurements from the laser diffraction instrument are shown in Figure S1.

The mass percentage of the seed crystals is only 10% of the total mass of the L-histidine in the solution (14% of the total mass of the final product mass considering the theoretical yield). Thus, most of the crystals at the end of the crystallization are expected to be formed during desupersaturation. The appearance of the peak at 20 μm is attributed to secondary nucleation, which is explained in detail in Section 3.3.

As the g-force on the reactor increases, the mode of the PSD increases from 19 at 1 g to 30 μm at 3 g. However, when the g-force is further increased, the mode of the distribution decreases to 22 μm at 4 g and 21 μm at 5 g. The change in the mode of the distribution at different g-levels is shown in Table 4. Table 4 also shows that the standard deviation of the

**Table 4. Mode and Standard Deviations of the PSDs at Different g-Levels**

| g-level | mode of distribution (μm) | standard deviation of distribution (μm) |
|---|---|---|
| 1 | 18.8 | 8.5 |
| 2 | 18.8 | 9.9 |
| 3 | 30.1 | 11.2 |
| 4 | 22.7 | 10.9 |
| 5 | 20.7 | 10.4 |

PSD increases from 8.5 μm at 1 g to 11 μm at 3 g, before reducing to 10.5 μm at 5 g. This indicates that with increasing g-level the PSD initially broadens, but the effect is non-monotonic. This shows that by crystallizing molecules in different gravity environments, it may be possible to achieve shifts in the PSD with the purpose of improving drug product performance.

Figure 10a−d shows the optical micrographs of samples grown at three different g-levels (1, 3, and 5 g). The optical micrographs confirm the broad features visible in the laser diffraction data across the sample, e.g., peaks at 20−30 and 180 μm. In addition, the appearance of the seed crystals is markedly different from that of the product particles generated at different g-levels. Optical micrographs are not as quantitative as laser diffraction data since a very small fraction of particles is sampled by the field of view of an optical image. Because of the limitations in quantifying PSD using static image analysis, PSD is quantified exclusively using laser diffraction data.

The hypergravity experiments at 1, 3, and 5 g were independently repeated on different days to assess the repeatability of the process. The results are shown in Figure 10e and indicate that the measured PSD is consistent at several g-levels. The coefficient of variation of the modes of the PSDS are 4.5, 7.6, and 7.4%, respectively, for 1, 3, and 5 g. Statistical analysis was also carried out on the modes of the PSD at each g-level using SAS JMP 17.0. The *p*-value for the pairwise difference of means of the modes across different g-levels is less


https://doi.org/10.1021/acs.cgd.3c01274
Cryst. Growth Des. XXXX, XXX, XXX−XXX

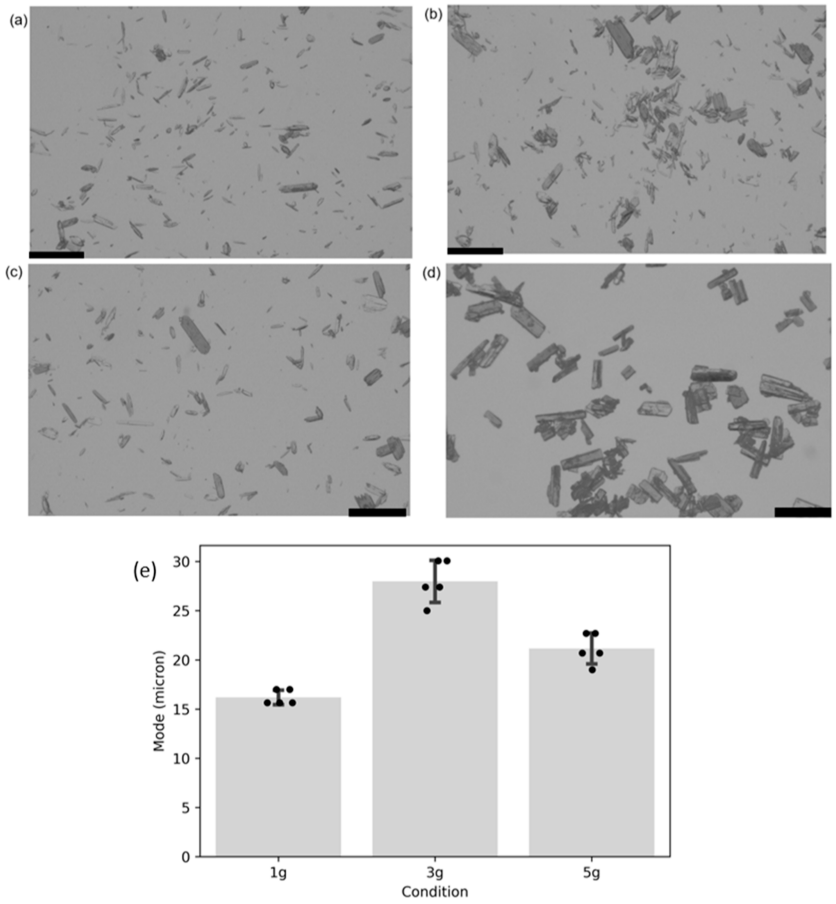


**Figure 10.** Optical micrographs of the seeded cooling crystallization of L-histidine at (a) 1, (b) 3, (c) 5 g, and (d) seed crystals. Scale bars, 500 $\mu$m; (e) bar plots indicating the mean mode of PSD along with individual modes overlaid as a function of the g-level. Error bars indicate standard deviation.

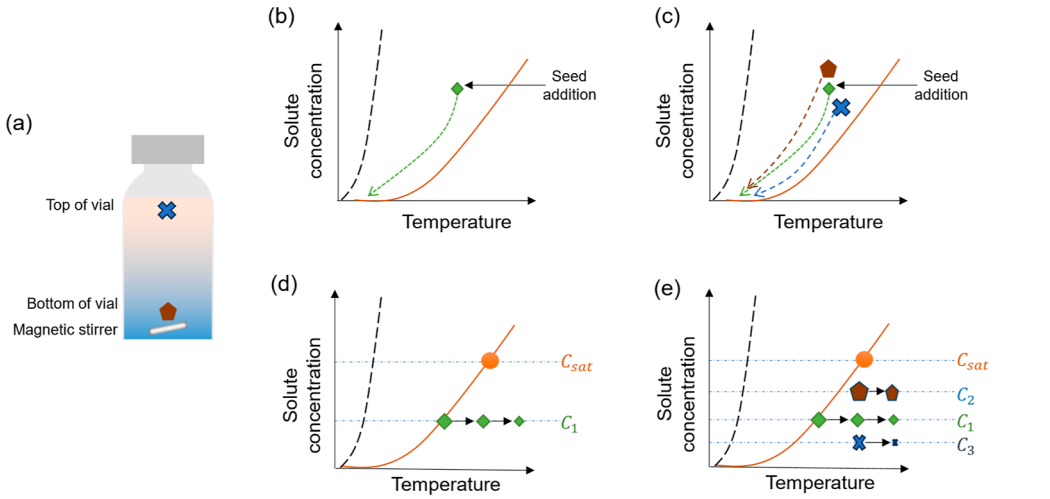


$$R_d = k_d(C_{sat} - C)^d$$

$$R_{d1} = k_d(C_{sat} - C_1)^d \quad C_2 > C_1 > C_3$$
$$R_{d2} = k_d(C_{sat} - C_2)^d$$
$$R_{d3} = k_d(C_{sat} - C_3)^d \quad R_{d2} < R_{d1} < R_{d3}$$

**Figure 11.** (a) Illustration of a vial used for centrifuge cooling crystallization experiments. The color indicates a gradient in concentration. Evolution of the system during cooling crystallization (b) in the case of a uniform concentration profile across the vial and (c) for a nonuniform concentration profile. Evolution of the system during a dissolution experiment for (d) a spatially homogeneous solution concentration and (e) when the solution concentration has a spatial gradient.


https://doi.org/10.1021/acs.cgd.3c01274
Cryst. Growth Des. XXXX, XXX, XXX−XXX

than 0.05. Thus, the null hypothesis that the modes are equivalent across g-levels can be rejected with >95% confidence. This indicates that a statistically significant shift in the mode with g-level was observed.

Additional characterization of the seed and product crystals was performed to assess the potential for polymorphic changes and unexpected changes in the seed crystal particle size due to breakage. The XRPD diffractograms of the seed and the product samples, together with reference diffraction patterns are shown in Figure S2. The diffractograms of both the seed and the product crystals are consistent with form A, and form B was not detected, indicating that polymorphic changes did not influence the observed PSD.

Breakage experiments were conducted with L-histidine seed crystals dispersed in ethanol. A detailed description of breakage experiments is provided in the Supporting Information. As shown in Figure S7, the shift of the PSD due to mechanical forces is small compared to the shift observed in the crystallization experiments during the centrifuge studies. Thus, breakage can be ruled out as a major contributing factor to the shift in the observed PSD for the Crystal16 centrifuge experiments. Thus, the fundamental mechanistic understanding of the crystallization phenomena observed in EasyMax experiments is still transferable to analyzing the experiments conducted in Crystal16.

**3.5. Mechanistic Hypothesis of the Effect of Gravity on Seeded Cooling Crystallization of L-Histidine.** The EasyMax experiments in Section 3.3 reveal that the crystallization process was dominated by secondary nucleation, which is also the most plausible mechanism for Crystal16 experiments.

Since the EasyMax experiments confirmed that the system lies within the metastable zone during the entire duration of the experiment, we do not need to consider primary nucleation as a possible mechanism. The hypothesis presented here considers secondary nucleation and crystal growth as the dominant mechanisms during desupersaturation. As crystals grow, they consume solute molecules, changing the local L-histidine concentration in the solution. Because transport is not instantaneous, spatial inhomogeneities arise,[50] with nonuniformities in concentration across the reactor driven by density differences. With increasing g-level, the lower and higher density regions undergo stratification, resulting in a spatial gradient in supersaturation across the container. This leads to the formation of a concentration boundary that moves to the bottom of the vial with time. This results in a spatial gradient of secondary nucleation and crystal growth rates with higher rates of nucleation and growth at higher supersaturation. At higher g-levels, the supersaturation is higher at the bottom of the solution and lower at the top of the solution (Figure 11a–c). Increasing the g-level to 3 g increases the size of the supersaturation gradient, forming regions of increased supersaturation at the bottom of the vial and regions of lower supersaturation at the top of the vial. In the higher supersaturation regions, both secondary nucleation rates and growth rates are increased, allowing the crystals generated to reach larger sizes and shifting the PSD to 30 $\mu$m.

Surprisingly, the trend reverses while further increasing the g level from 3 to 5 g. This may be attributed to the spatial distribution of the supersaturation gradient. While at an apparent g-level of 5 g, the peak supersaturation may be expected to be higher than at 3 g, the supersaturated region is more tightly confined to a limited volume of the container. In addition, particles tend to concentrate toward the bottom of the vial due to the high g-forces. Since at higher supersaturations secondary nucleation supersedes crystal growth,[51] the mode of the final PSD is lower at 5 g compared to 3 g.

The ultimate balance of the change of the nucleation and growth rate is a complex function of the density of the solvent, the apparent g-level, the PSD of the seed crystals, and the secondary nucleation and growth kinetics. This needs to be considered on a case-by-case basis since it is highly dependent on the API and the solvent, and no generalized rule can be proposed for a new molecule and solvent system.

**3.6. Dissolution Experiments.** Seeded dissolution experiments were performed to further validate the hypothesis that spatial concentration gradients drive changes in the observed PSD. If the concentration is homogeneous throughout the vial, changes in the PSD during dissolution would be expected to be independent of the g-level. However, if a spatial variation in concentration forms differently at different g-levels, then shifts in the PSD during dissolution will be different at different g-levels, Figure 11d illustrates the case where the concentration is homogeneous spatially across the vial. The rate of crystal dissolution is given by eq 8, where $k_d$ and $d$ are dissolution constants, $C_{sat}$ is the saturation concentration, and $C$ is the concentration of the L-histidine in solution. If the solution concentration is spatially uniform, the rate of dissolution will be uniform throughout the solution.

$$R_d = k_d(C_{sat} - C)^d \tag{8}$$

However, if the concentration is not spatially homogeneous throughout the solution, then the rate of dissolution will also have a spatial gradient. Figure 11e shows three operating points in the solution distributed spatially—one near the top of the vial, one at the middle of the vial, and one at the bottom. The solution concentration has a spatial gradient, with lowest concentration at the top and highest concentration at the bottom. Since the rate of dissolution is dependent on the difference between the solution concentration and the solubility limit of L-histidine, particles are expected to experience the fastest rate of dissolution at the top of the vial and the slowest rate of dissolution at the bottom of the vial. Thus, a spatial gradient in the supersaturation can lead to different particle sizes at the end of the experiment.

Figure 12 shows the volume-based PSDs for the dissolution experiments described in Section 2.10. The modes of the distributions are listed in Table 5 for readability. After 20 min of dissolution, the mode of the volume-based PSD shifts to the left from 185 to 47, 44, and 39 $\mu$m at 1, 3, and 5 g, respectively, as shown in Figure 12a. The trends with increasing g-levels indicate that the rate of dissolution increases with increasing centrifugal forces, with the enhancement explained by the formation of low-concentration regions that promote faster dissolution. At 40 min of dissolution (Figure 12b), the modes are 40, 22.5, and 39 $\mu$m at 1, 3, and 5 g, respectively. While the left shift of the first two modes is consistent with the notion that increasing g-levels increases spatial gradients and promotes enhanced dissolution, the sample that undergoes dissolution at 5 g undergoes little shift from 20 to 40 min, which is attributed to sedimentation effects bringing the crystals in equilibrium with localized high concentration region at the bottom of the vial.

The observed modes of the volume-based PSD at 40 min as a function of g-level (Table 5) exhibit the reverse of the trend observed in Table 4 during the seeded desupersaturation


https://doi.org/10.1021/acs.cgd.3c01274
Cryst. Growth Des. XXXX, XXX, XXX−XXX

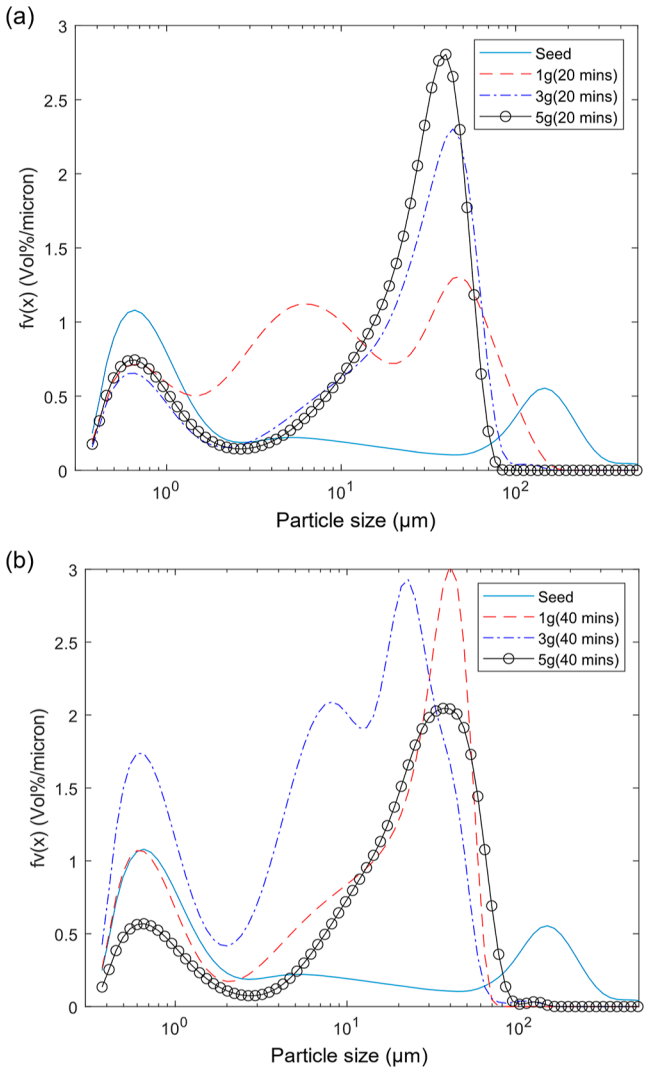


**Figure 12.** Volume-based PSD at (a) 20 and (b) 40 min for different g-levels.

**Table 5. Observed Modes during Dissolution Studies**

| condition (g) | prior to dissolution ($\mu$m) | 20 min ($\mu$m) | 40 min ($\mu$m) |
|---|---|---|---|
| 1 | 185 | 47 | 40 |
| 3 | 185 | 44 | 22.5 |
| 5 | 185 | 39 | 39 |

experiments. The observation of nonmonotonic behavior across both crystallization and dissolution studies helps support the hypothesis that observed changes in PSDs are driven by concentration gradients and that the behavior is a result of multiple competing dynamics.

It is to be noted that although the hypothesis of supersaturation-mediated changes in crystallization under hypergravity has been proposed in the literature before,[50] there was limited experimental supporting evidence available. This work confirms the hypothesis through a combination of (a) quantitative measurements of PSDs with laser diffraction, (b) crystallization experiments with in situ PAT tools for enhanced process understanding, and (c) dissolution experiments at variable g-levels to further probe supersaturation-mediated changes in crystallization outcomes in hypergravity.

In addition, while previous hypergravity studies primarily focused on protein molecules at g-levels often in the 1000 to 10,000 g range and often found no effects of gravity at less than 100 g, this work shows that at the 2 mL scale, small-molecule crystallizations have different outcomes depending on the effective gravity level. This study reveals that gravity-driven supersaturation gradients can arise even while stirring at 800 rpm on the 2 mL scale, which impacts a wide range of studies on typical screening platforms such as the Crystal16.

It is to be noted that the transferability of crystallization mechanisms across the Crystal16 reactor and EasyMax is case-dependent, i.e., it depends on the mechanical properties of the product crystals and the sensitivity of the crystallization mechanisms to the reactor hydrodynamics. Based on the experiments performed, we can conclude that secondary nucleation is the primary mechanism for L-histidine cooling crystallization that leads to the observed PSDs for both the EasyMax and Crystal16 experiments.

## 4. CONCLUSIONS

Seeded cooling crystallization of L-histidine was performed at different g-levels using a centrifuge. The measured shifts in the PSD were nonmonotonic with increasing g-levels. Experiments were run in the EasyMax reaction calorimeter with in situ PAT tools to quantify the MSZW and the sensitivity of the Raman spectra to changing L-histidine concentration and temperature. A chemometric model was built to calculate the L-histidine concentration as a function of the instantaneous Raman spectra and the solution temperature. In situ PAT data from the Blaze probe revealed secondary nucleation to be the dominant mechanism of crystallization. The evolution of the system in the phase diagram showed rapid desupersaturation initially, followed by slower desupersaturation at the end due to the Arrhenius nature of the growth kinetics. A hypothesis was developed that explains changes in the product PSD as a function of g-level through the formation of spatial variations in concentration and supersaturation. Dissolution experiments were designed to support the hypothesis that concentration gradients drive changes in crystallization outcomes. The possibility of particle breakage significantly influencing the measured PSD was ruled out by experiments discussed in the Supporting Information. The hypergravity experiments also show that gravity affects the crystallization process even when the solution is stirred at high rpm, highlighting that gravity likely plays a significant role in many small-molecule crystallization processes. Since particle size has a significant impact on dissolution rate and oral bioavailability, as has been well documented in the literature,[52−55] accounting for the effect of gravity may be especially important for APIs whose crystallization behavior is sensitive to spatial concentration gradients. Variable gravity platforms are well-positioned to rapidly generate data sets that show how gravity impacts the crystallization of small-molecule pharmaceuticals, paving the way to achieve better control over crystallization and highlighting opportunities for improved process control in microgravity.

## ■ ASSOCIATED CONTENT

### Supporting Information

The Supporting Information is available free of charge at https://pubs.acs.org/doi/10.1021/acs.cgd.3c01274.



https://doi.org/10.1021/acs.cgd.3c01274
Cryst. Growth Des. XXXX, XXX, XXX−XXX

Additional characterization (pH of solution before and after crystallization experiment), XRPD of seed and product crystals, unseeded nucleation experiments, Raman spectra for L-histidine, dynamic image analysis of seed and product crystals, solubility measurement of L-histidine in water, and investigation of the breakage of L-histidine in ethanol (PDF)

## AUTHOR INFORMATION


### Corresponding Author

**Adrian Radocea** − *Varda Space Industries, El Segundo, California CA-90245, United States;* orcid.org/0000-0002-4496-2573; Email: adrian@varda.com

### Author

**Kanjakha Pal** − *Varda Space Industries, El Segundo, California CA-90245, United States*

Complete contact information is available at: https://pubs.acs.org/10.1021/acs.cgd.3c01274


### Notes

The authors declare the following competing financial interest(s): K. Pal and A. Radocea are employees of Varda Space Industries and may own Varda Space Industries stock.

## ACKNOWLEDGMENTS

The authors would like to thank Pamela Smith, Stephan D. Parent, Dale Purcell, and Brett Cowans of Improved Pharma LLC for their useful discussions on crystallization mechanisms. The authors would like to thank Andrew McCalip, Jeff Anderson, Haley Bauser, and Mark Ragains from Varda Space Industries for their help with the centrifuge and helpful discussions about crystallization experiments. The authors would like to thank Michael Vynnycky, Doireann O'Kiely, and Kevin Moroney of the Science Foundation of Ireland Research Center for Pharmaceuticals (SSPC) under the European Regional Development: 12/RC/2275_P2 for their useful discussions about hypergravity.

## REFERENCES


(1) Reichert, P.; Prosise, W.; Fischmann, T. O.; Scapin, G.; Narasimhan, C.; Spinale, A.; Polniak, R.; Yang, X.; Walsh, E.; Patel, D.; Benjamin, W.; Welch, J.; Simmons, D.; Strickland, C. Pembrolizumab microgravity crystallization experimentation. *npj Microgravity* **2019**, *5* (1), 28.

(2) Sahin, E.; Deshmukh, S. Challenges and considerations in development and manufacturing of high concentration biologics drug products. *J. Pharm. Innov.* **2020**, *15* (2), 255−267.

(3) Ghosh, I.; Gutka, H.; Krause, M. E.; Clemens, R.; Kashi, R. S. A systematic review of commercial high concentration antibody drug products approved in the US: formulation composition, dosage form design and primary packaging considerations. *mAbs* **2023**, *15* (1), 2205540.

(4) Above and beyond: Our research returns to space. https://www.bms.com/life-and-science/news-and-perspectives/protein-crystallization-experiment-in-space-for-improved-patient-care.html (accessed Sept 14, 2023).

(5) Shaping the Future of Drug Development with Space-based Protein Crystallization. https://www.bms.com/life-and-science/science/innovative-science-of-space-based-protein-crystallization.html (accessed Sept 14, 2023).

(6) Examining Nanoparticle Formation in Microgravity for Improved Therapeutic Cancer Vaccines. https://www.issnationallab.org/examining-nanoparticle-formation-in-microgravity-for-improved-therapeutic-cancer-vaccines/ (accessed Sept 14, 2023).

(7) Monoclonal Antibody Stability in Microgravity-Formulation Study. https://www.nasa.gov/mission_pages/station/research/experiments/explorer/Investigation.html?#id=7914 (accessed Sept 14, 2023).

(8) Potential of microgravity: How companies across sectors can venture into space. https://www.mckinsey.com/industries/aerospace-and-defense/our-insights/the-potential-of-microgravity-how-companies-across-sectors-can-venture-into-space (accessed Sept 14, 2023).

(9) Fujiwara, M.; Nagy, Z. K.; Chew, J. W.; Braatz, R. D. First-principles and direct design approaches for the control of pharmaceutical crystallization. *J. Process Control* **2005**, *15* (5), 493−504.

(10) Choong, K. L.; Smith, R. Optimization of batch cooling crystallization. *Chem. Eng. Sci.* **2004**, *59* (2), 313−327.

(11) Mota, F. L.; Carneiro, A. P.; Queimada, A. J.; Pinho, S. P.; Macedo, E. A. Temperature and solvent effects in the solubility of some pharmaceutical compounds: Measurements and modeling. *Eur. J. Pharm. Sci.* **2009**, *37* (3−4), 499−507.

(12) Li, H.; Kawajiri, Y.; Grover, M. A.; Rousseau, R. W. Modeling of nucleation and growth kinetics for unseeded batch cooling crystallization. *Ind. Eng. Chem. Res.* **2017**, *56* (14), 4060−4073.

(13) Kubota, N.; Doki, N.; Yokota, M.; Sato, A. Seeding policy in batch cooling crystallization. *Powder Technol.* **2001**, *121* (1), 31−38.

(14) Nagy, Z. K. Model based robust control approach for batch crystallization product design. *Comput. Chem. Eng.* **2009**, *33* (10), 1685−1691.

(15) Yang, Y.; Pal, K.; Koswara, A.; Sun, Q.; Zhang, Y.; Quon, J.; McKeown, R.; Goss, C.; Nagy, Z. K. Application of feedback control and in situ milling to improve particle size and shape in the crystallization of a slow growing needle-like active pharmaceutical ingredient. *Int. J. Pharm.* **2017**, *533* (1), 49−61.

(16) Li, W.; Rielly, C. D.; Benyahia, B. Targeting Desired Particle Size for Improved Dissolution and Manufacturability of Mefenamic Acid. *Chem. Proc.* **2022**, *9* (1), 1−9.

(17) Liversidge, G. G.; Cundy, K. C. Particle size reduction for improvement of oral bioavailability of hydrophobic drugs: I. Absolute oral bioavailability of nanocrystalline danazol in beagle dogs. *Int. J. Pharm.* **1995**, *125* (1), 91−97.

(18) Pharma Looks to Outer Space to Boost Drug R&D; The Scientist. https://www.the-scientist.com/bio-business/pharma-looks-to-outer-space-to-boost-drug-rd-68183 (accessed Sept 14, 2023).

(19) McDowell, J. C. The low earth orbit satellite population and impacts of the SpaceX Starlink constellation. *Astrophys. J.* **2020**, *892* (2), L36.

(20) Vekilov, P. G. Protein crystal growth - Microgravity aspects. *Adv. Space Res.* **1999**, *24* (10), 1231−1240.

(21) Strelov, V. I.; Kuranova, I. P.; Zakharov, B. G.; Voloshin, A. E. crystallization in space: results and prospects. *Crystallogr. Rep.* **2014**, *59* (6), 781−806.

(22) Kundrot, C. E.; Judge, R. A.; Pusey, M. L.; Snell, E. H. Microgravity and macromolecular crystallography. *Cryst. Growth Des.* **2001**, *1* (1), 87−99.

(23) Snell, E. H.; Helliwell, J. R. Microgravity as an environment for macromolecular crystallization-an outlook in the era of space stations and commercial space flight. *Crystallogr. Rev.* **2021**, *27* (1), 3−46.

(24) Mcpherson, A.; Greenwood, A.; Day, J. The effect of microgravity on protein crystal growth. *Adv. Space Res.* **1991**, *11* (7), 343−356.

(25) Lorber, B. Virus and protein crystallization under hypergravity. *Cryst. Growth Des.* **2008**, *8* (8), 2964−2969.

(26) Dimitrov, I.; Nanev, C. N. Sedimentation as a tool for crystallization from protein mixtures. *Cryst. Res. Technol.* **2006**, *41* (11), 1063−1066.

(27) Zhou, Q.; Li, R.; Wang, J. X.; Du, J.; Qu, J.; Zhang, C.; Zhang, P.; Chen, J. F.; Li, C. High-Gravity-Tuned Synthesis of Uniformly

Distributed Silver Bismuth Chromate Semiconductor Crystals. *Cryst. Growth Des.* **2023**, *23* (1), 380−387.
(28) Yang, H.; Huang, L.; Zhang, F.; Karde, V.; Yang, Z.; Heng, J. Y. Y. Gravity on crystallization of lysozyme: slower or faster? *Cryst. Growth Des.* **2019**, *19* (12), 7402−7410.
(29) Esmonde-White, K. A.; Cuellar, M.; Uerpmann, C.; Lenain, B.; Lewis, I. R. Raman spectroscopy as a process analytical technology for pharmaceutical manufacturing and bioprocessing. *Anal. Bioanal. Chem.* **2017**, *409* (3), 637−649.
(30) Yousuf, M.; Frawley, P. J. Secondary Nucleation from Nuclei Breeding and Its Quantitative Link with Fluid Shear Stress in Mixing: A Potential Approach for Precise Scale-up in Industrial Crystallization. *Org. Process Res. Dev.* **2019**, *23* (5), 926−934.
(31) Agrawal, S. G.; Paterson, A. H. J. Secondary nucleation: mechanisms and models. *Chem. Eng. Commun.* **2015**, *202* (5), 698−706.
(32) Bosetti, L.; Mazzotti, M. Study of secondary nucleation by attrition of potassium alum crystals suspended in different solvents. *Cryst. Growth Des.* **2020**, *20* (4), 2570−2577.
(33) Barrett, P.; Glennon, B. Characterizing the metastable zone width and solubility curve using Lasentec FBRM and PVM. *Chem. Eng. Res. Des.* **2002**, *80* (7), 799−805.
(34) EasyMax 102 Advanced Thermostat system. https://www.mt.com/us/en/home/products/L1_AutochemProducts/chemical-synthesis-reactor-systems/EasyMax-Synthesis-Reactor.html (accessed Jan 07, 2023).
(35) BlazeMetrics user manual. https://www.blazemetrics.com/specifications (accessed Sept 01, 2023).
(36) Supriya, S.; Sivan, S.; Srinivasan, K. Nucleation Control and Separation of Stable and Metastable Polymorphs of L-histidine Through Novel Swift Cooling Crystallization Process. *Cryst. Res. Technol.* **2018**, *53* (3), 1700239.
(37) Agimelen, O. S.; Hamilton, P.; Haley, I.; Nordon, A.; Vasile, M.; Sefcik, J.; Mulholland, A. J. Estimation of particle size distribution and aspect ratio of non-spherical particles from chord length distribution. *Chem. Eng. Sci.* **2015**, *123* (2), 629−640.
(38) Wantha, L. Determination of Nucleation and Growth Mechanisms of the B Polymorph of L-Histidine by Induction Time Measurement. *Chem. Eng. Technol.* **2016**, *39* (7), 1289−1294.
(39) Kongsamai, P.; Wantha, L.; Flood, A. E.; Tangsathitkulchai, C. In-situ measurement of the primary nucleation rate of the metastable polymorph B of L-histidine in antisolvent crystallization. *J. Cryst. Growth* **2019**, *525* (1), 125209.
(40) Mehta, M.; Naffa, R.; Maidment, C.; Holmes, G.; Waterland, M. Raman and ATR-FTIR spectroscopy towards classification of wet blue bovine leather using ratiometric and chemometric analysis. *J. Leather Sci. Eng.* **2020**, *2* (1), 3−15.
(41) Soto, R.; Verma, V.; Sadeghi, M.; Rasmuson, Å. C. Ketoprofen solubility in pure organic solvents using in situ FTIR and UV-Vis and analysis of solution thermodynamics. *Org. Process Res. Dev.* **2021**, *25* (11), 2403−2414.
(42) Karimi-Jafari, M.; Soto, R.; Albadarin, A. B.; Croker, D.; Walker, G. In-line Raman spectroscopy and chemometrics for monitoring cocrystallisation using hot melt extrusion. *Int. J. Pharm.* **2021**, *601* (2), 120555.
(43) Soto, R.; Verma, V.; Lynch, A.; Hodnett, B. K.; Rasmuson, Å. C. Crystal Growth Kinetics of Pharmaceutical Compounds. *Cryst. Growth Des.* **2020**, *20* (12), 7626−7639.
(44) Regression in Matlab. https://www.mathworks.com/help/matlab/ref/mldivide.html (accessed Sept 19, 2023).
(45) Pandalaneni, K.; Amamcharla, J. K. Focused beam reflectance measurement as a tool for in situ monitoring of the lactose crystallization process. *J. Dairy Sci.* **2016**, *99* (7), 5244−5253.
(46) Tiwari, V.; Walker, G.; Ranade, V. V. Particle Breakage Using Wet Mill, Ultrasonic, and Hydrodynamic Cavitation. *Cryst. Growth Des.* **2023**, *23* (12), 8620−8636.
(47) Ahmed, B.; Brown, C. J.; McGlone, T.; Bowering, D. L.; Sefcik, J.; Florence, A. J. Engineering of acetaminophen particle attributes using a wet milling crystallisation platform. *Int. J. Pharm.* **2019**, *554*, 201−211.
(48) Saw, M. H.; Hishamuddin, E.; Chong, C. L.; Yeoh, C. B.; Lim, W. H. Effect of polyglycerol esters additive on palm oil crystallization using focused beam reflectance measurement and differential scanning calorimetry. *Food Chem.* **2017**, *214*, 277−284.
(49) Jordens, J.; Canini, E.; Gielen, B.; Van Gerven, T.; Braeken, L. Ultrasound assisted particle size control by continuous seed generation and batch growth. *Crystals* **2017**, *7* (7), 195−220.
(50) Nanev, C. N.; Dimitrov, I.; Hodjaoglu, F. Hypergravity as a Crystallization Tool. *Ann. N.Y. Acad. Sci.* **2006**, *1077* (1), 172−183.
(51) Xu, S.; Hou, Z.; Chuai, X.; Wang, Y. Overview of secondary nucleation: From fundamentals to application. *Ind. Eng. Chem. Res.* **2020**, *59* (41), 18335−18356.
(52) Jinno, J. I.; Kamada, N.; Miyake, M.; Yamada, K.; Mukai, T.; Odomi, M.; Toguchi, H.; Liversidge, G. G.; Higaki, K.; Kimura, T. Effect of particle size reduction on dissolution and oral absorption of a poorly water-soluble drug, cilostazol, in beagle dogs. *J. Controlled Release* **2006**, *111* (1−2), 56−64.
(53) Ghosh, I.; Bose, S.; Vippagunta, R.; Harmon, F. Nanosuspension for improving the bioavailability of a poorly soluble drug and screening of stabilizing agents to inhibit crystal growth. *Int. J. Pharm.* **2011**, *409* (1−2), 260−268.
(54) Dong, Y.; Ng, W. K.; Shen, S.; Kim, S.; Tan, R. B. H. Preparation and characterization of spironolactone nanoparticles by antisolvent precipitation. *Int. J. Pharm.* **2009**, *375* (1−2), 84−88.
(55) Sun, J.; Wang, F.; Sui, Y.; She, Z.; Zhai, W.; Wang, C.; Deng, Y. Effect of particle size on solubility, dissolution rate, and oral bioavailability: evaluation using coenzyme $Q_{10}$ as naked nanocrystals. *Int. J. Nanomed.* **2012**, *7* (2), 5733−5744.


https://doi.org/10.1021/acs.cgd.3c01274
*Cryst. Growth Des.* XXXX, XXX, XXX−XXX